56th 3AF International Conference on Applied Aerodynamics
28 – 30 March 2022, Toulouse - France

FP22-AERO2022-Petropoulos

Numerical aerodynamic performance assessment of HLFC wing configurations using far-field drag analysis

Ilias Petropoulos[(1)], Thomas Streit[(2)], Thomas Kilian[(3)] and Martin Kruse[(4)]

[(1)] *ONERA, 8 rue des Vertugadins, F-92190 Meudon, France, ilias.petropoulos@onera.fr*
[(2)] *DLR, Lilienthalplatz 7, D-38108 Braunschweig, Germany, Th.Streit@dlr.de*
[(3)] *DLR, Lilienthalplatz 7, D-38108 Braunschweig, Germany, Thomas.Kilian@dlr.de*
[(4)] *DLR, Lilienthalplatz 7, D-38108 Braunschweig, Germany, Martin.Kruse@dlr.de*

ABSTRACT

This paper presents the aerodynamic performance analysis of realistic large passenger aircraft equipped with a Hybrid Laminar Flow Control (HLFC) system. To this purpose, the design of two HLFC aircraft geometries is first outlined, both designed by DLR based on an Airbus HLFC variant of the XRF-1 geometry. Numerical simulations were performed with the TAU RANS solver of DLR, using an extension of its LST-based automatic transition prediction capability for cases with boundary layer suction. Aerodynamic performance assessment was then performed using the ONERA *ffd72* far-field drag analysis software, allowing comparisons between configurations in terms of phenomenological drag components. The overall assessment of the different configurations considers both the laminarization benefit using HLFC technology compared to a fully turbulent reference aircraft and the performance penalty when the HLFC wing is operated under fully turbulent conditions. Results of the analysis are consistent with the geometry modifications and the flow physics, highlighting an overall HLFC benefit via the reduction of friction and viscous pressure drag components. A wave drag penalty, inherent to the laminarization of the outer wing upper surface, is identified in the original HLFC geometry designed by DLR and reduced in its further improved version.

1. INTRODUCTION

The environmental impact of civil aviation coupled with the growth of aircraft traffic have motivated the orientation of regulations towards restrictions for more fuel-efficient aircraft. To this end, the Advisory Council for Aviation Research and innovation in Europe (ACARE) has introduced stringent requirements aiming at a reduction of the environmental footprint of the aviation sector [1]. Goals of the European Vision FlightPath 2050 address, among others, the reduction of pollutant emissions and perceived noise of flying aircraft, sustainability (alternative fuels, recycling) and atmospheric impact. To achieve these ambitious objectives, improved aircraft components, and even disruptive technologies, must be developed both individually and collectively, with respect to their integration on the aircraft. The role of aerodynamic design methods can thus contribute to the reduction of pollutant emissions by the design of more fuel-efficient aircraft (i.e. reduced consumption for a given mission), in particular by reducing aerodynamic drag.

The subject of aerodynamic drag is however complex. Despite the existence of numerous approaches to drag reduction at a theoretical or elementary level, it is not often the case in terms of their application at an industrial level. Civil transport aircraft in particular make the integration of disruptive technologies difficult in practice, due to the need for manufacturing adaptations, design methodology validation, as well as cost, maintenance, certification and safety concerns. A promising way to achieve an important reduction of aerodynamic drag, under a reasonable increase of configuration complexity, is to delay transition in order to maintain a laminar flow over parts of the aircraft surface.

The delay of transition of the flow from laminar to turbulent can be achieved by Hybrid Laminar Flow Control (HLFC) systems [2]. These couple the application of airfoil geometries adapted to natural laminar flow principles [3-4] with laminar flow control. Over the recent years, an evaluation of the impact of HLFC technology for large passenger aircraft is being carried out within the frame of the HLFC-WIN project, funded by the Clean Sky 2 Joint Undertaking under the European Union's Horizon 2020 research and

innovation programme. This programme is a research collaboration between Aernnova, DLR, ONERA and SONACA group, with Airbus as an industrial partner. In order to perform this assessment, an integral approach is followed, combining aerodynamic and structural studies, manufacturing, system design and integration (WIPS, Krueger flaps, suction system), wind-tunnel testing, small-scale demonstrators and a large-scale ground-based-demonstrator (GBD). These numerical and experimental studies are performed within a complete validation and verification process. In particular, this project aims at reaching a TRL4 (technology readiness level) on integrated component level for HLFC technology on transonic wings of mid- to long-haul transport aircraft.

The present paper focuses on the evaluation of HLFC benefits solely on aerodynamic performance. The assessment presented in this paper was performed based on numerical simulations of realistic aircraft configurations at a cruise operating point, including engines with power-on boundary conditions. In particular, the design process and analysis presented in this paper concern the designed wing geometry of the GBD of the HLFC-WIN project. The extended transition prediction capability of the TAU Code for HLFC designs was recently developed in German Aeronautical Research Program LuFo In.Fly.Tec/ Applaus.

The paper is structured as follows. At a first step, the aircraft configuration under investigation is presented, followed by a description of the methods used and the HLFC wing design process. A numerical aerodynamic performance assessment is then presented for the HLFC configurations designed by DLR within the HLFC-WIN project. In particular, comparisons are performed between an initial geometry and a further improved one, aiming at improving performance based on results of the far-field drag analysis of the initial geometry. In addition to free transition computations, a refined assessment is presented, accounting for turbulent wedges between the suction panel segments of the final HLFC system. Finally, an outlook on further improvement in terms of physical modelling for HLFC configurations is given, followed by conclusions.

2. DESCRIPTION OF THE AIRCRAFT CONFIGURATION & SCOPE OF GEOMETRY MODIFICATIONS

The studies carried out in this work use the Airbus XRF-1 research large passenger aircraft as a reference geometry [5-6]. This geometry contains the fuselage, wing, nacelle, pylon, flap-track fairings and vertical tail plane. A perspective view of the aircraft is shown in Figure 1. CFD computations and far-field analyses consider only half of the aircraft geometry. The geometry corresponds to a target 1g flight shape.

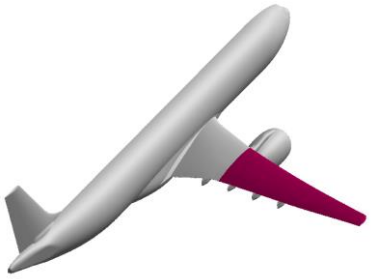

Figure 1. Perspective view of the XRF-1 aircraft highlighting the wing region considered for geometry modifications and HLFC application.

The nominal flight conditions at cruise are the following: $M_\infty = 0.83$, $C_L = 0.5$, $\mathrm{Re} \approx 47 \cdot 10\text{^}6$ and a flight altitude of 36,000 ft. For the far-field drag analysis presented in this paper, the priority was put on the accurate aerodynamic performance analysis at cruise conditions. For this reason, with the exception of fully turbulent computations of the HLFC geometries, off-design aerodynamic performance was not considered.

Geometry modifications were restricted to the outer part of the wing, outboard of the leading edge kink and close to the engine position (colour-shaded region in Figure 1), i.e. for span position $\eta \geq 0.319$. A more detailed description of the design requirements is given in section 4.1.

At a first step, a HLFC variant of the XRF-1 aircraft was designed by Airbus. The aerodynamic design studies of DLR were then performed using this geometry as a starting point. The HLFC wing surface geometry selected for the HLFC-WIN ground base demonstrator is denoted GBD-DLR-2. A further design is the GBD-DLR-3 geometry, which improves the aerodynamic performance of the GBD-DLR-2 geometry. The initial geometry used in the design is the HLFC variant of the XRF-1 aircraft designed by Airbus, denoted as the Airbus 1g HLFC geometry. For a consistent far-field performance analysis among the different configurations, the Airbus 1g HLFC case will not be considered, since it has a smaller spanwise thickness distribution than the reference geometry and the new DLR designs.

3. DESIGN AND SIMULATION METHODS

The numerical simulations carried out in the course of this work can be classified into HLFC wing design and analysis tasks. The following sections describe the methodology and the numerical methods used in each case.

3.1. Design method

The DLR inverse transonic 3D design method was used to design the HLFC outer wing [8]. This allows the

design of adapted wing sections using user-specified target pressure distributions. The inverse design method is an integrated module of the DLR FLOWer code [9] for block structured meshes.
The used target pressure distributions are generated with the aim to increase laminar extent and/or reduce shock strength. In the case of HLFC target pressure distributions, also the shape of the pressure distribution in the nose suction region is important. A HLFC pressure distribution presents a suction peak within the suction region. The height and extension of this peak has to be chosen carefully, considering its influence on transition position and shock strength. Furthermore, the change of the suction peak with off-design conditions has to be considered.
The CFD meshes used for the HLFC wing design use a reduced level of geometrical representation without flap track fairings and engine pylon. They comprise separate wing, body and engine meshes and CFD solutions are obtained using the chimera (overset mesh) technique.
Together with these simplifications, the inverse design method has the advantage that it is a robust, efficient and accurate CFD method, ideal for a large number of design iterations and extensive off-design analysis.

3.2. CFD analysis for complete configurations

For the final analysis of the designed HLFC configurations, the full configuration including flap-track fairings and engine pylon is considered. For this purpose, the wing sections designed with the inverse design process are transferred into a CAD model of the complete aircraft. The CAD model forms the basis for the analysis CFD mesh, which was created using the mesh generator SOLAR [10]. With a resolution of about 30E6 mesh points, this mesh is much finer than the design meshes.
For the CFD simulations, DLR's flow solver TAU [7] was used. TAU solves the Reynolds-averaged Navier-Stokes equation (RANS) on a cell vertex, finite volume formulation. For the spatial discretization, a central Jameson scheme with matrix dissipation is applied. Time integration is performed with an implicit backward Euler scheme, using LU-SGS. Turbulence modelling was performed with the Spalart-Allmaras SA-negative model.
TAU's iterative automatic transition prediction module [11] is employed to evaluate the local laminar/turbulent transition position for a user-defined number of spanwise stations. At each station, pressure distributions and geometrical data are extracted from the current CFD solution and passed to a differential boundary layer solver. Employing the local conical wing assumption, the solver calculates the local boundary layer profiles. The transition location is predicted by means of local linear stability analysis and a 2-N factor transition criterion, calibrated for HLFC application. The new transition locations for all stations investigated form a transition polyline. The transition polyline is then passed back to the CFD solver to distinguish laminar and turbulent parts of the flow. The process of CFD calculation and transition prediction is repeated iteratively. Convergence is usually reached within six iterations. To allow for the treatment of HLFC wing sections, the basic transition prediction module was enhanced to read-in user specified suction distributions. Consideration of the suction distributions in the boundary layer solver then allows for transition prediction for HLFC configurations.
Details on methods and codes involved in the transition prediction module are given in the following section.

3.3. Methods and tools employed for stability analysis and transition prediction

Despite the emergence of more sophisticated stability analysis methods, LST remains the preferred technical tool for stability analysis in computationally intensive design and analysis activities outlined here. Both the design process and the final analysis use the STABTOOL program suite [12-13] for transition prediction based on local linear stability theory (LST).
For the stability analysis of 3D wing boundary layers, the assumption of spanwise locally conical flow conditions is introduced at first. This assumption allows a numerically efficient calculation of the laminar boundary layer profiles per wing section. The boundary layer code *coco* [13] was used to calculate compressible, conical flow boundary layer profiles. *Coco* supports calculations with prescribed boundary layer suction, requiring a special pre-processor provided by G. Schrauf.
To calculate the growth rates of Tollmien-Schlichting (TS) and cross flow (CF) instability modes the local linear stability solver *lilo* was employed. To solve the LST eigenvalue problem, a fixed frequency and fixed propagation direction approach is used for TS waves, while a fixed frequency/fixed wavenumber approach is chosen for CF waves. TS mode evaluation is restricted to a propagation direction of $\Psi=0°$, i.e. along the group velocity direction . For cross flow, only stationary modes (f=0Hz) are considered. Separate N-factors for TS and CF modes are obtained by integrating the respective growth rates along the group velocity direction.
To predict the transition location, a 2-N factor transition criterion is used. The N-factor limit curve was adapted for HLFC design purposes. In addition, a Re_Θ criterion is evaluated to check for possible attachment line transition.

4. DESIGN OF HLFC WING CONFIGURATIONS

In this section, the aerodynamic design of the wing surface of the ground-based demonstrator will be

described. All results shown here correspond to the complete aircraft configuration. They are restricted to the cruise design point. The aerodynamic performance results for the designed geometries will be described separately in Chapter 6.

4.1. Design requirements

Aerodynamic requirements: Design flow conditions are: the cruise design point given in chapter 2. Off-design is considered in the range: $0.45 \leq CL \leq 0.55$, $0.81 \leq M_\infty \leq 0.85$. For all flow conditions the active engine boundary conditions (fan intake and primary/secondary stream exhausts) provided by Airbus for the cruise point were used. For the cruise point, the design should not significantly alter the circulation distribution of the Airbus HLFC geometry. This reduces the influence of induced drag changes to overall aerodynamic performance.

Geometry requirements: A detailed HLFC design of the outer wing ($\eta \geq 0.319$) is performed. Thickness requirements are: maintain or increase front spar airfoil thickness and maximum airfoil thickness of the Airbus-HLFC geometry.

Transition position: For HLFC-WIN the laminar region is restricted to the upper side. For the shape design, a generic suction distribution was used. It was defined based on the suction distribution used by Airbus for its HLFC design. For consistency with the Airbus results, the transition position was obtained by DLR using incompressible stability analysis and flight incompressible critical N_{TS}/N_{CF} values [14]. However, it is important to mention that for this Mach number: a) a free flight calibration of critical N-factors is not available b) compressible and incompressible stability analysis may lead to designs with different geometry and performance potential [15].

4.2. Design methodology and results

In the early stage of the design, CFD results were obtained for wing-body meshes and wing-body-engine meshes. Comparison with CFD results obtained for the analysis mesh, showed that: a) for the inverse design it was sufficient and necessary to include the engine in the design process, b) pylon and FTF's could be neglected since their influence was reduced to a local span region.

The geometry of the GBD-DLR-2 design was obtained in 2 steps since in comparison to the XRF-1 geometry, the Airbus HLFC 1g geometry has a decreased thickness distribution in the outer wing, the first design step was to modify the thickness distribution. For that purpose, the lower side was changed in order to regain thickness. As shown in Figure 2 this leads to a GBD-DLR-2 pressure distribution with a decreased minimum pressure for the lower side. This shape modification was done without altering the upper wing surface pressure distribution and the local lift value. In comparison to the initial Airbus HLFC design, the maximum airfoil thickness was increased by $\Delta t/c=1\%$ in the outer wing for dimensionless span $\eta > 0.4$. In the second design step, the upper side was considered for the free transition case and target pressure distributions were generated in order to increase the laminar extent of the Airbus HLFC geometry. For that purpose, target pressure distributions were used in the design which did not change the shock strength, but changed the nose suction peak and the pressure gradient.

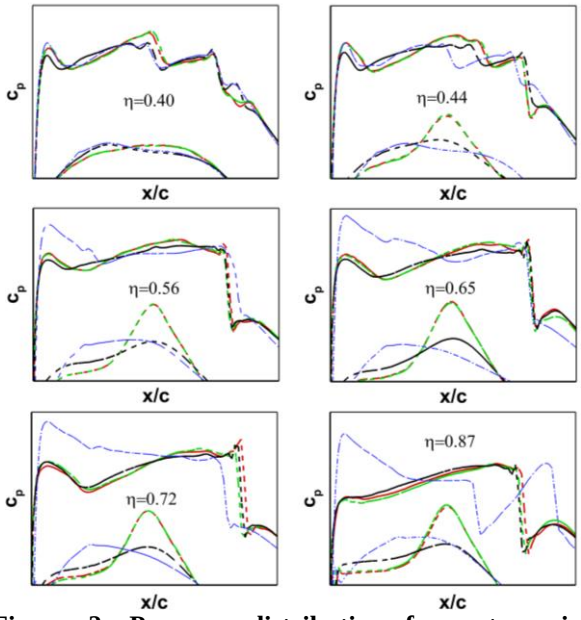

Figure 2. Pressure distribution for outer wing sections. Results for geometries with free transition for Airbus HLFC 1g (black), GBD-DLR-2 (green) and GBD-DLR-3 (red) and for reference XRF-1 geometry (blue) with turbulent boundary layer.

Figure 2 shows the pressure distribution of the finally designed GBD-DLR-2 geometry using these target pressure distributions. In Figure 2 this is compared to results obtained for the Airbus HLFC 1g (free transition) and the XRF-1 (turbulent) cases. The leading edge region of the HLFC design airfoils generally exhibits lower leading edge radii and reduced curvature. As a result, this leads to a reduced pressure gradient in this region on the pressure side. Overall, both HLFC geometries exhibit a more regular acceleration of the flow up to roughly 30%-40% of the chord on the pressure side than the reference wing, a favourable effect for the preservation of a laminar region. On the suction side and at the outboard part of the wing, the pressure coefficient evolutions of HLFC wings are quite different from that on the reference configuration. The acceleration following the most forward weak recompression (which is overall weaker for the HLFC wings) is favourable for the delay of transition. In addition, the upstream recompression can limit the intensity of shockwaves despite the acceleration over an

important portion of the chord. The reference turbulent wing overall shows an arrangement of multiple shock waves. HLFC wings on the other hand aim at extending the laminar region by presenting a more progressive acceleration, which leads to a single shock wave around 60% of the chord. This is clearly visible closer to the wing tip, at η=0.87, where the reference geometry results in a first shock closer the mid-chord position, followed by a decompression and a second shock further downstream. HLFC geometries however result in a more progressive acceleration up to a single shock formed in an intermediate position with respect to the two shocks of the turbulent wing. Concerning the comparison between fully turbulent and laminar/turbulent computations on the HLFC wings, an important difference is observed at the shockwave location. Differences on the pressure coefficient are already observed at η=0.40. The shockwave position is moved further downstream in the laminar/turbulent cases, compared to the fully turbulent computation of each corresponding HLFC configuration.

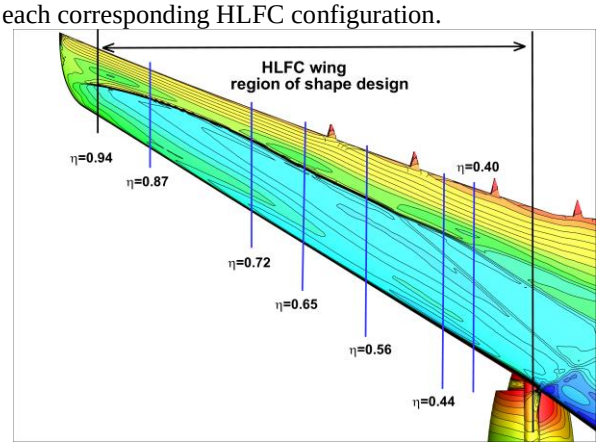

Figure 3. Upper surface pressure distribution contours for the GBD-DLR-2 geometry.

The GBD-DLR-2 design is also influenced by the flow properties of the fixed shape inner wing. As discussed above, the inner wing shows a complex shock system. Unfortunately, the leading edge part of the λ-shock (see Figure 4) that originates from the inner turbulent wing (wing root section) partially restricts the extension of laminar boundary layer in the outer wing part (HLFC wing part). This is seen in the pressure distribution for sections η=0.40 and η=0.44 (see Figure 2), where the more upwind placed shock will lead to a transition. In addition to the λ-shock, Figure 3 and Figure 4 show an inner wing shock originating at the inboard pylon wing intersection.

The transition position for the DLR-HLFC designs is given in Figure 4. Note that the GBD-DLR-2 geometry has extended the laminar extent of the Airbus HLFC geometry case by an additional 1.7% of the wing surface.

As will be shown in the far-field drag analysis in chapter 6, the GBD-DLR-2 configuration showed an increase of wave drag in comparison to the reference and the Airbus HLFC 1g geometries. This wave drag increase occurred around a region of span position n=0.6. This occurs despite the GBD-DLR-2 and the Airbus HLFC configuration showing no significant difference in shock strength in the pressure distributions.

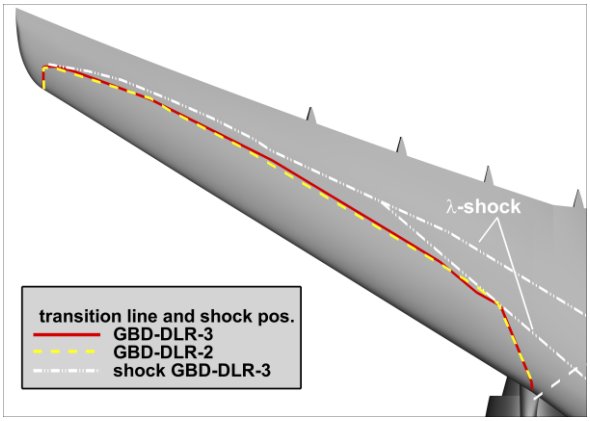

Figure 4. Free transition position for HLFC outer wing and shock position.

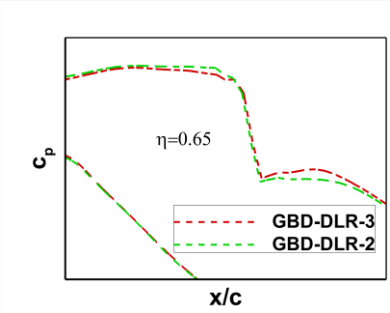

Figure 5. Comparison of pressure distribution in the shock region for η=0.65. Solutions for turbulent boundary layer with analysis mesh

Therefore, an additional geometry was designed denoted GBD-DLR-3. Target pressure distributions were used for the GBD-DLR-3 case with a slightly larger recompression between the transition position and the shock. As shown in Figure 5 for the pressure distribution of wing section η=0.65, the finally designed GBD-DLR-3 shows this property. Furthermore, the GBD-DLR-3 geometry was designed in such a way that the angle of attack for which the cruise design point lift value is achieved is closer to the angle of attack at which this occurs for the Airbus HLFC 1g geometry. Thus, differences to the latter case in induced drag and pressure distribution for inner wing and body should be reduced. In comparison to the GBD-DLR-2 geometry, the GBD-DLR-3 shows an improved aerodynamic performance (see chapter 6) and a slightly increased laminar boundary layer extent (see Figure 4). Results show that the circulation distributions for the designed geometries are very similar to the circulation

distribution of the Airbus HLFC 1g configuration (results not shown here). The latter differs from the one of the XRF-1 geometry.
Besides the HLFC designs described here, further designs which consider the inner wing and the tip region of the HLFC-WIN configuration were performed. They will be described in a future contribution which considers the design and analysis of the HLFC-WIN configurations in more detail.

5. FAR-FIELD DRAG ANALYSIS METHOD

Near-field drag coefficients are computed by performing an integration of forces on the aircraft skin. On the other hand, a far-field evaluation of drag components is performed through integrals in the flow field. This allows a phenomenological breakdown of drag into physical components, namely viscous, wave and induced drag. Furthermore, a far-field evaluation of drag is more accurate than its near-field counterpart, thus also allowing for a quantification of spurious drag production.
Far-field drag analyses are performed using the *ffd72* post-processing software of ONERA. The formulation and employed methodology are described in [16-17]. The far-field method relies on an accurate physics-based definition of control volumes for the integration of viscous pressure, wave and induced drag. The aforementioned software and methodology have been extensively applied in the research and industry over the past decades.
Near-field drag is defined as the sum of pressure and friction drag:

$$CD_{nf} = CD_p + CD_f \quad (1)$$

Far-field drag on the other hand is defined as the sum of the viscous, wave and induced drag components:

$$CD_{ff} = CD_v + CD_w + CD_i \quad (2)$$

where:

$$CD_v = CD_{vp} + CD_f \quad (3)$$

Spurious drag production is inherent to numerical computations, and is a product of numerical approximation (e.g. mesh discretization, artificial dissipation). A quantification of spurious drag is made possible through the difference of the two drag calculations:

$$CD_{sp} = CD_{nf} - CD_{ff} \quad (4)$$

Finally, the far-field drag extraction method provides the drag balance:

$$CD_p + CD_f = CD_v + CD_w + CD_i + CD_{sp} \quad (5)$$

Additional variables and performance measures are computed in the case of motorized configurations (see e.g. [16]), in particular specific drag/thrust bookkeeping methods. A view of integration volumes is shown in Figure 6.

Figure 6. Perspective view of the integration volumes for viscous pressure (grey) and wave drag (black).

6. AERODYNAMIC PERFORMANCE ANALYSIS

This section presents the aerodynamic performance analysis of the aircraft configurations designed by DLR and described in section 4. The geometries considered in this study are the original HLFC geometry designed by DLR (denoted as GBD-DLR-2) and its improved counterpart (denoted as GBD-DLR-3) which was designed by DLR taking into account results of the far-field drag analysis of the original GBD-DLR-2 version.

6.1. Analysis based on a free transition approach

In laminar/turbulent computations, suction is taken into account in transition prediction but this only influences the laminar region extent, as the boundary conditions employed do not include active suction across the surface. Still, the laminarization of the boundary layer naturally has a significant effect on skin friction. Figure 7 shows a skin friction distribution at a 60% wingspan position for the five different cases. The reduction of skin friction for the laminar region of the flow is clearly visible, and extends across an important part of the chord at this spanwise position. As expected, this advantage no longer exists in fully turbulent flow over the same geometries. Between the two HLFC wings, the GBD-DLR-3 shows a slightly lower skin friction at the end of the laminar region.

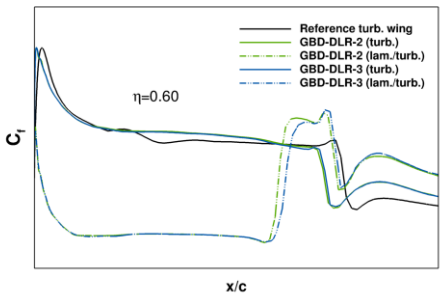

Figure 7. Friction coefficient across the upper wing surface at η=0.60 for the reference aircraft and its HLFC variants in fully turbulent and laminar / turbulent (free transition) conditions.

Table 1: Near-field and far-field drag coefficient increments (w.r.t. the reference XRF-1 aircraft) computed with the ffd72 software for the two HLFC geometries in fully turbulent and laminar/turbulent conditions at cruise. The laminar surface percentage is computed with respect to the wing surface, excluding the pylon and FTFs.

Geometry	Transition type	AoA(°)	ΔCDp	ΔCDf	ΔCDvp	ΔCDw	ΔCDi	ΔCDsp	ΔCDff	Laminar surface [%]
XRF-1	Turbulent	2.634	-	-	-	-	-	-	-	-
GBD-DLR-2	Turbulent	2.781	+2.05%	-0.15%	-1.79%	+99.77%	+0.85%	-20.90%	+2.27%	-
	Free transition	2.682	-1.13%	-4.69%	-16.92%	+85.29%	-0.20%	-10.17%	-2.86%	14.26 %
GBD-DLR-3	Turbulent	2.745	+1.55%	-0.35%	-1.64%	+83.91%	+0.33%	-17.51%	+1.59%	-
	Free transition	2.637	-1.85%	-5.01%	-19.19%	+70.11%	-0.52%	-19.21%	-3.71%	14.42 %

Global lift and near-field/far-field drag coefficient increments of the HLFC configurations are presented in Table 1. Increments are computed with respect to the corresponding coefficient value of the reference XRF-1 aircraft. Note also that computations were performed at approximately the same lift coefficient, which results in a different angle of attack. At a first step, the two HLFC geometries are compared against the reference XRF-1 in fully turbulent conditions. This corresponds to the worst-case scenario in terms of laminar area extent, but remains important for the overall aircraft performance assessment as such conditions may occur in a number of flight events and conditions. Concerning the fully turbulent computations, friction drag is similar for the three configurations (difference less than 0.5%), the total near-field drag difference being thus mainly attributed to the skin pressure drag component. The difference of pressure drag with respect to the reference aircraft case is important for the two HLFC geometries at fully turbulent conditions. A far-field drag decomposition of the total drag force highlights that the main contribution to this is a notable increase of wave drag. This pressure drag penalty in turbulent conditions is reduced on the GBD-DLR-3, because of geometry modifications aiming at reducing the wave drag identified in the far-field drag analysis of the GBD-DLR-2 geometry. Still, relative variations are generally increased, as absolute wave drag levels are low on such a reference transonic wing. An increase of induced drag is also observed, albeit at a lower level compared to that in terms of wave drag. It is interesting to note that, even in fully turbulent conditions, the HLFC geometries yield a reduced viscous pressure drag with respect to the reference XRF-1 aircraft. The overall drag of the aircraft evaluated by the far-field analysis is however higher than the reference.

On the other hand, the laminar/turbulent computations with a free transition approach indicate that both geometries exhibit an improved overall performance with respect to the XRF-1 aircraft, taking into account the laminarization introduced by the geometry modifications and the HLFC system. In terms of near-field values, drag reduction is obtained both in terms of pressure and friction drag. Whereas the laminarization benefit is often attributed to the friction drag component only, these results highlight that an important benefit is also obtained in terms of viscous pressure drag. The absolute increments for these two components are of the same order of magnitude. This benefit is found to be even more important in the improved GBD-DLR-3 configuration. The wave drag increase compared to the reference aircraft remains present in laminar/turbulent computations, but at a lower level compared to fully turbulent conditions. Furthermore, an additional benefit is obtained for both HLFC geometries in terms of induced drag. The improved aerodynamic performance of the GBD-DLR-3 is overall apparent, as its total far-field drag benefit with respect to the reference is notably higher than that of the GBD-DLR-2. It is also important to note that the modifications introduced for the reduction of the wave drag penalty do not degrade aerodynamic performance in terms of any individual drag component with respect to the GBD-DLR-2.

The computed drag coefficient increments are consistent with the modifications introduced in each of the HLFC geometries. Finally, the absolute value of spurious drag was found to remain at a similar level between the different cases. This was found to be low, which is the reason for the large proportional differences in the tabulated data.

The above results highlight the importance of an accurate far-field drag assessment. First, an appropriate far-field drag analysis can provide a considerably increased precision compared to a near-field evaluation of drag, and thus a more accurate prediction of the drag benefit due to laminarization. On the other hand, the phenomenological decomposition is essential to the improvement of the aerodynamic design and the accurate understanding of the physical mechanisms involved. Looking only into near-field drag components one could indeed consider that the benefit of laminarization is mainly obtained by a reduction of friction drag. As expected, a far-field breakdown shows that the benefit of laminarization is in fact distributed between the friction and viscous pressure drag components. In other words, when working solely based

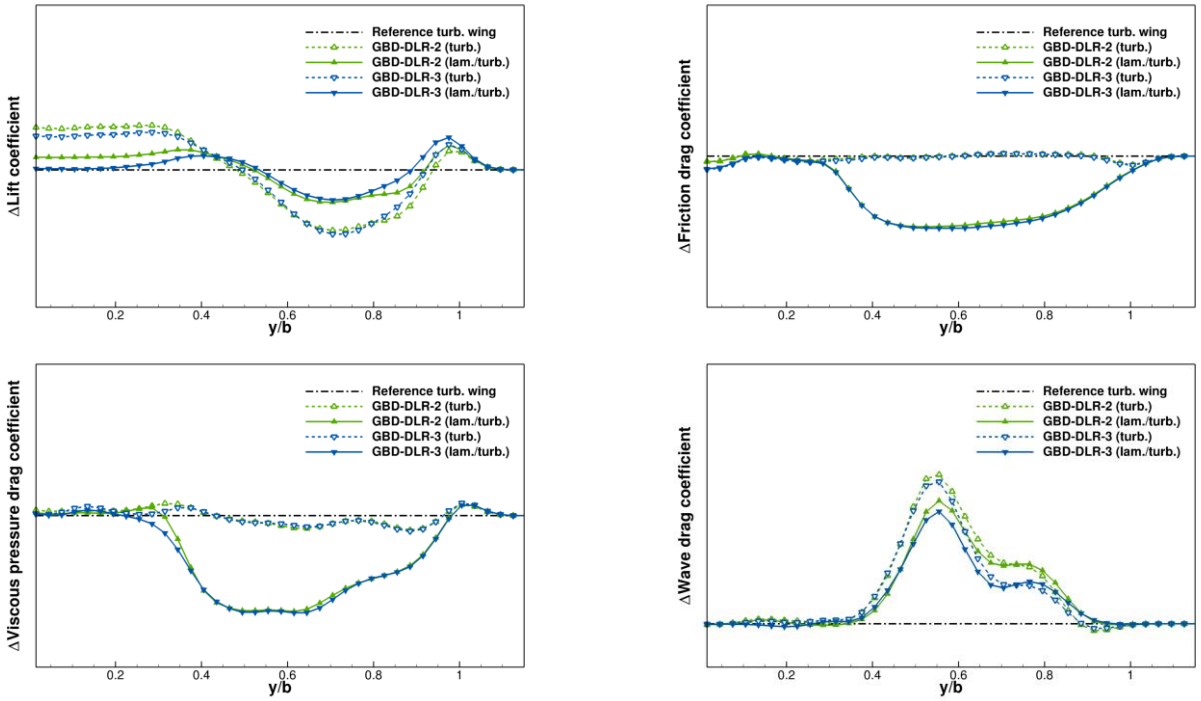

Figure 8: Approximate spanwise distribution of near-field and far-field coefficient increments with respect to the reference XRF-1 aircraft, computed with the ffd72 software.

on the pressure drag value, the viscous pressure drag benefit can be masked by a wave drag or induced drag contribution. The far-field drag analysis thus indicates the possibility of separately addressing the issue of the wave drag penalty in this case. This importance is demonstrated by the improved performance of the GBD-DLR-3 geometry, compared to the GBD-DLR-2. An improvement is observed both in terms of a larger drag benefit due to laminarization and in a reduction of the drag penalty if the wing is operated in fully turbulent conditions.

The identification of areas responsible for performance gains, or losses, is thus important in order to efficiently guide aerodynamic design. Such an indication can be given by the approximate spanwise distribution of aerodynamic coefficients, presented in Figure 8. The lift coefficient distribution shows a slight transfer of load towards the inboard part of the wing for the two HLFC designs. This is more apparent on fully turbulent conditions and is mitigated on the laminar/turbulent computations. Minor modifications are also noted on the friction and viscous pressure drag components near the engine position. Furthermore, in both distributions, the benefit of laminarity is clear on the outboard part of the wing. Finally, the wave drag increase identified in Table 1 is clearly apparent in the spanwise distribution of wave drag, and is particularly localized on the outboard part of the wing. Trends are overall similar between the GBD-DLR-2 and GBD-DLR-3 configurations, whereas differences are consistent with the global drag coefficient increments presented in Table 1.

6.2. Adapted transition prediction taking into account technology effects

The following step towards a more reliable evaluation of the HLFC aerodynamic performance benefit is a more accurate prediction of the laminar region. For this reason, additional computations were performed using a refined definition of the laminar region, accounting for technology effects consistent with the HLFC systems designed in the HLFC-WIN project. Regarding laminar/turbulent transition, the suction magnitude was reduced without compromising the laminar region extent and the suction area was adjusted to the spanwise variation in the front spar location. Turbulent wedges were introduced at segment boundaries, where a 15° opening angle assumption was made. Finally, the transition line from stability analysis results in nine sections across all four HLFC segments was superimposed with the aforementioned turbulent wedges and lead to a more realistic laminar area extent. It should also be noted that this limits the inboard extent of the laminar region with respect to the previous free transition computations. This is because free-transition computations were performed before the exact definition of the panel extent in the finalized HLFC system.

The laminar region modification in this updated transition computation can be seen in Figure 9, which shows a comparison of skin friction and the transition line for the two types of laminar/turbulent computations. The same figure also shows a comparison of the transition line on the wing upper surface for all the

laminar/turbulent computations presented above. This comparison gives a clearer view of the laminar region reduction when considering a limited spanwise extent of the laminar region, as well as introducing turbulent wedges between segment boundaries. As shown earlier (see Figure 4), the geometry modifications introduced in the GBD-DLR-3 geometry are also confirmed to have a minimal but beneficial effect on the extent of the laminar region, compared to the DLR-2.

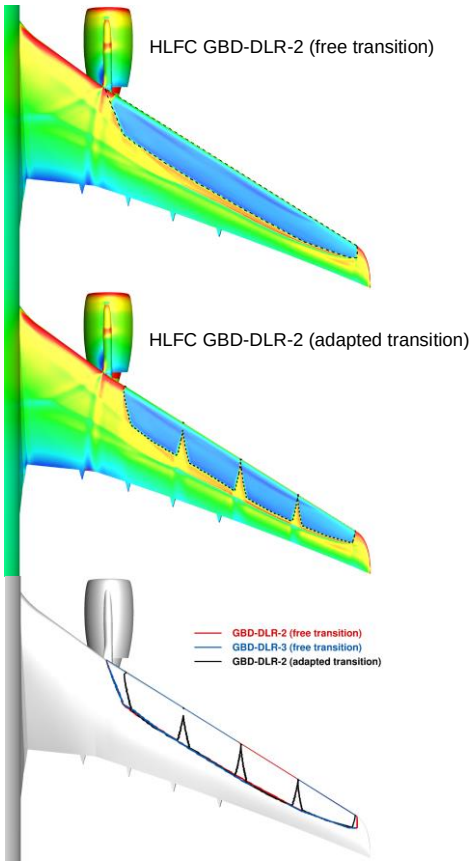

Figure 9. Magnitude of skin friction coefficient for the HLFC GBD-DLR-2 variant with free or adapted transition (top/middle) and transition line comparison for the laminar/turbulent computations (bottom).

The influence of the adapted transition prediction on the aerodynamic performance is summarized in Table 2. Most near-field and far-field coefficients are penalized by the reduced laminar region due to increased viscous drag. Induced drag also shows a minor increase, whereas wave drag is slightly reduced with respect to the free transition computation. The overall penalty when considering a more realistic laminar region compared to the computation with free transition is shown to be reduction of the drag benefit by 0.29% with respect to the total far-field drag of the reference XRF-1 aircraft. In terms of the spanwise distribution of drag components, modifications due to the adaptation of the transition prediction were found to be small, but consistent with the overall values presented in Table 2.

6.3. Further improvement to physical modelling

The presented simulation methodology for HLFC configurations considers the effect of boundary layer suction only in the context of transition prediction. In the RANS simulation, however, only laminar and turbulent flow regions are distinguished and the effect of suction on the boundary layer development is not accounted for. Since the area of the suction surfaces is relatively small in relation to the total wetted area, it is assumed that the influence of this simplification on the total resistance is negligible in a first approximation.
The inclusion of boundary layer suction into RANS simulations and a quantification on HLFC performance is the subject of ongoing work at DLR. The results will be presented in an upcoming paper.

7. CONCLUSIONS

This paper presents an aerodynamic performance assessment of realistic HLFC wing configurations, designed by DLR within the Clean Sky 2 HLFC-WIN project. Aerodynamic performance has been assessed using the *ffd72* far-field drag analysis software of ONERA, based on fully turbulent and laminar/turbulent CFD computations at a cruise operating point including engines with power-on boundary conditions.
Two HLFC wing geometries have been analysed, both designed by DLR based on a HLFC variant of the XRF-1 research geometry, designed by Airbus. The HLFC region is restricted to the outer wing. The first corresponds to the original geometry for the large-scale ground-based demonstrator of the HLFC-WIN project. The second is a further improved version of this geometry aiming at improving its aerodynamic performance, considering results of the far-field drag analysis of the original version. Far-field drag analysis shows that HLFC designs introduce an important drag

Table 2: Influence of a refined transition prediction on near-field and far-field drag coefficient increments (w.r.t. the reference XRF-1 aircraft) computed with the ffd72 software for the two HLFC geometries at cruise conditions. The laminar surface percentage is computed with respect to the wing surface, excluding the pylon and FTFs.

Geometry	Transition type	AoA(°)	ΔCDp	ΔCDf	ΔCDvp	ΔCDw	ΔCDi	ΔCDsp	ΔCDff	Laminar surface [%]
GBD-DLR-2	Free transition	2.682	-1.13%	-4.69%	-16.92%	+85.29%	-0.20%	-10.17%	-2.86%	14.26 %
	Adapted transition	2.691	-0.94%	-4.50%	-16.32%	+81.84%	-0.13%	-13.56%	-2.57%	13.32 %

benefit, both in terms of the friction and viscous pressure drag components. A wave drag penalty, inherent to the laminarization of the outer wing upper surface, is also identified. The estimated benefit of the improved HLFC geometry with respect to the original XRF-1 aircraft is estimated to be in the order of 3.71% at cruise conditions. This benefit is however slightly reduced (reduction in the order of 0.29% for the original HLFC geometry) when considering an adapted transition approach, which takes into account technology integration effects (exact suction panel placement, and turbulent wedges between segments). Both approaches are in good agreement, but the latter is essential at a second design step, where the drag prediction difference between the two approaches lies beyond the error margin for a realiable technology evaluation.

These observations highlight that the physical insight and quantification of the influence of the different mechanisms behind drag reduction, as well as the use of numerical methods of adequate fidelity, are essential steps towards the design and implementation of HLFC technology in future passenger aircraft.

ACKNOWLEDGEMENTS

This work was funded by the European Union within the frame of the HLFC-WIN project. This project is part of the Clean Sky 2 Joint Undertaking under the European Union's Horizon 2020 research and innovation programme (Grant agreements CS2-GAM-2018-LPA-AMD-807097-38 and CS2-GAM-2020-LPA-AMD-945583-11). The HLFC code development was funded by German Federal Ministry for Economic Affairs and Energy within the German Aeronautical Research Program LuFo V-3/2018-2022 In.Fly.Tec/Aplaus under grant agreement no 20A1705C.

REFERENCES

1. Advisory Council for Aviation Research and Innovation in Europe (ACARE), Strategic Research and Innovation Agenda (SRIA), https://www.acare4europe.org/sria, accessed on 12th January 2022.

2. Krishnan, K. S. G., Bertram, O., & Seibel, O. (2017). Review of hybrid laminar flow control systems. *Progress in Aerospace Sciences*, 93, 24-52.

3. Hue, D., Vermeersch, O., Bailly, D., Brunet, V., & Forte, M. (2015). Experimental and numerical methods for transition and drag predictions of laminar airfoils. *AIAA Journal*, 53(9), 2694-2712.

4. Hue, D., Vermeersch, O., Duchemin, J., Colin, O., & Tran, D. (2018). Wind-tunnel and CFD investigations focused on transition and performance predictions of laminar wings. *AIAA Journal*, 56(1), 132-145.

5. Kroll, N., Abu-Zurayk, M., Dimitrov, D. *et al.* DLR project Digital-X: towards virtual aircraft design and flight testing based on high-fidelity methods. *CEAS Aeronautical Journal* **7,** 3–27 (2016).

6. Carini, M., Blondeau, C., Fabbiane, N., Meheut, M., Abu-Zurayk, M., Feldwisch, J. M., Caslav, I.. & Merle, A. (2021). Towards industrial aero-structural aircraft optimization via coupled-adjoint derivatives. In *AIAA Aviation 2021 Forum*, Paper 2021-3074.

7. D. Schwarmborn, T. Gerhold, R. Heinrich, "The DLR TAU-Code: Recent Applications in Research and Industry", *Proceedings of European Conference on Computational Fluid Dynamics ECCOMAS CFD 2006*, Delft, Netherlands

8. Streit, T., Hoffrogge, C., DLR transonic inverse design code, extensions and modifications to increase versatility and robustness, *The Aeronautical Journal*, 2017, **121**, (1245), pp 1733-1757.

9. Kroll, N. and Fassbender, J.K. MEGAFLOW – Numerical Flow Simulation for Aircraft Design, *Notes on Numerical Fluid Mechanics and Multidisciplinary Design (NNFM)* vol. **89**, Springer Verlag, Closing Presentation DLR Project MEGAFLOW Braunschweig (de), 10–11 January 2002.

10. SOLAR 15.3.7 M Leatham, S Stokes, J A Shaw, J Cooper, J Appa, T A Blayloc. Automatic Mesh Generation for Rapid-Response Navier-Stokes Calculations, AIAA Paper 2000-2247, 2000.

11. Krimmelbein, N., Krummbein, A., Industria-lization of the Automatic Transition Prediction in the DLR TAU Code, Notes on Numerical Fluids Mechanics and Multidisciplinary Design, book series (NNFM, volume 123), Computational Flight Testing, pp. 89-98, 2013.

12. Schrauf, G., LILO 2.1 – Users Guide and Tutorial, GSSC Technical Report, July 2006.

13. Schrauf, G., COCO – A Program to Compute Velocity and Temperature Profiles for Local and Nonlocal Stability Analysis of Compressible, Conical Boundary Layers with Suction, ZARM Technik Report, November 1998.

14. Schrauf G., "Large Scale Laminar Flow Test Evaluated with Linear Stability Theory, Journal of Aircraft". Vol. 41, No. 2 ,2004.

15. Streit, T., Seitz, A., Hein, S., Kunze, P. (2020) NLF Potential of Laminar Transonic Long Range Aircraft. AIAA Aviation 2020 Forum, 15-19. June 2020, USA Virtual Event, doi: 10.2514/6.2020-2748.

16. Van Der Vooren, J., and Destarac, D., "Drag/thrust analysis of jet-propelled transonic transport aircraft; definition of physical drag components," *Aerospace Science and Technology*, Vol. 8, No. 6, 2004, pp. 545–556.

17. Destarac, D., "Far-Field / Near-Field Drag Balance and Applications of Drag Extraction in CFD, In: CFD-based Aircraft Drag Prediction and Reduction", VKI Lecture Series 2003, Von Karman Institute for Fluid Dynamics, Rhode Saint Genèse, February 3-7, 2003, National Institute of Aerospace, Hampton (VA), November 3-7, 2003.